Pushing the limits: Resolving paleoseawater signatures in nanoscale fluid inclusions by atom probe tomography

S. D. Taylor,[1]* D. D. Gregory,[2] D. E. Perea,[3] L. Kovarik,[1] J. B. Cliff,[3] T. W. Lyons[4]*

[1]Physical and Computational Sciences Directorate, Pacific Northwest National Laboratory, Richland, WA 99354, USA

[2]Department of Earth Sciences, University of Toronto, Toronto, ON M5S 3B1, Canada

[3]Earth and Biological Sciences Directorate, Pacific Northwest National Laboratory, Richland, WA 99354, USA

[4]Department of Earth and Planetary Sciences, University of California, Riverside, CA 92521, USA

*Corresponding authors:

Sandra D. Taylor, Physical Sciences Division, Pacific Northwest National Laboratory, Richland, WA 99354 USA, (509) 371-6374, sandra.taylor@pnnl.gov

Timothy W. Lyons, Department of Earth Sciences, University of California, Riverside, CA 92521 USA, (951) 827-3106, timothy.lyons@ucr.edu

Revision prepared for *Earth and Planetary Science Letters*

Abstract

New insight into the geochemistry of ancient environments can be gained through structural and chemical analyses of nanometer-scale features within minerals. Here, we present recent developments using atom probe tomography (APT) enabling direct visualization of nanoscale fluid inclusions trapped within pyrite (FeS_2) and thereby chemical characterization of remnant seawater. Pyrite framboids (spherical clusters of nanocrystals) were sampled from the Middle Devonian Leicester Pyrite Member (New York). Scanning transmission electron microscopy shows low density features distributed within the pyrite (<4 nm in size). Three-dimensional chemical visualization and analysis by APT reveals these to be nanoscale fluid inclusions preserving the elemental signatures of the water column in which the framboids formed, as alkalis consistent with seawater including Na, K, Mg, and Ca are identified. Further, within the inclusions Mg/Ca is measured to be ~0.6±0.2 – consistent with conditions for calcite-dominated seawater existing in the Middle Devonian. The results and approach developed in this study show the potential to reconstruct paleoenvironmental conditions from coupled elemental and structural analyses of nanoscale fluid inclusions.

Keywords

Fluid inclusion; pyrite; seawater chemistry; atom probe tomography

1. Introduction

Reconstructing Earth's environmental conditions in the geologic past can be achieved through analysis of fluid inclusions trapped during growth of minerals at or near Earth's surface (Goldstein, 2001; Lowenstein et al., 2001). For instance, the chemistry of fluid inclusions within halite from marine deposits can track secular changes in seawater chemistry, including oscillations across time (Balthasar and Cusack, 2015). Despite many past successes, the full wealth of information about paleoenvironmental conditions possible from analysis of fluid inclusions remains largely untapped given the constraints on material systems, inclusions size, and techniques available for inclusion analysis. Transparent minerals like halite (NaCl) and calcite ($CaCO_3$) have historically been emphasized, as inclusions are observable using optical techniques (Brennan and Lowenstein, 2002), although this approach limits coverage of the stratigraphic record. Further, characterization is often limited to at least micrometer-sized inclusions as required by conventional techniques, such as laser ablation inductively coupled mass spectrometry (LA-ICP-MS) and scanning electron microscopy energy dispersive spectroscopy (SEM-EDS) (Johnson and Goldstein, 1993; Lowenstein et al., 2001). While nanometer-scale (referred to as nanoscale here) fluid inclusions are prevalent (Bodnar and Samson, 2003), the capacity in which paleoenvironmental conditions can be inferred is largely overlooked given the limited knowledge and techniques available for such efforts.

In this study we seek to overcome these long-standing barriers, presenting new capabilities and insight into fluid inclusion analysis at the atomic level. High-resolution microscopy techniques such as scanning transmission electron microscopy (STEM) can identify inclusions as microstructural defects, although compositional analyses are limited due to projection issues (i.e., characterization of three-dimensional (3D) features is based on two-dimensional (2D) renderings) and its low chemical-sensitivity (e.g., inability to resolve light elements like H) (Viti and Frezzotti, 2001; Deditius et al., 2009; Parish et al., 2015). Conversely, atom probe tomography (APT) is a recognized and powerful analytical technique for the chemical characterization of clusters/precipitates within solids in 3D with sub-nanometer-scale, barring fine-scale aberrations due ion trajectory overlaps and local magnification effects (Marquis and Vurpillot, 2008; Marquis and Hyde, 2010; Gault et al., 2021)(refs therein). The recent advent in the analyses of nanoscale defects and their interpretation enabled by these techniques have provided unprecedented insight into geologic processes, from crystal growth/recrystallization mechanisms (Fougerouse et al., 2016; Taylor et al., 2018; Taylor et al., 2019) to interpreting geochronologic events (Moser et al., 2013; Valley et al., 2014; Peterman et al., 2016; White et al., 2017). The utility of APT in resolving inclusions has only been recently demonstrated in minerals, such as pyrite (FeS_2) (Dubosq et al.,

2020; Reddy et al., 2020; Daly et al., 2021; Dubosq et al., 2021; Liu et al., 2022), although deep insight into the chemistry and paleoenvironmental significance of these features has not been achieved.

Here, we build on these analytical advances to directly visualize and characterize nanoscale water-filled inclusions within pyrite. Identification and microstructural characterization of the inclusions was achieved by STEM while APT was used to measure the chemical composition within the inclusions, with the goal of tracking paleo-seawater chemistry. We chose a framboidal pyrite specimen from the Devonian period with a well-known geologic history for context (Formolo and Lyons, 2007). In general, chemical signatures within the nanoscale fluid inclusions and compositional analyses, such as Mg/Ca ratios, are consistent with previous studies (Horita et al., 2002; Demicco et al., 2005). This study provides new insight into nanoscale fluid inclusion analyses that may enable exploration of paleoenvironmental conditions across a broad range of environments and timescales. Additionally, our analyses using pyrite present the potential to expand Mg/Ca measurements from evaporitic environments to major sedimentary minerals, thereby further improving ancient records for seawater chemistry.

2. Material and Methods

2.1 Specimen information

Pyrite framboids were sampled from the Leicester Pyrite Member (LPM) in the Devonian Appalachian Basin (New York, *ca.* 390 Ma) (Baird and Brett, 1986). The LPM is a sedimentary lag deposit that crops out over hundreds of kms in upstate New York, comprised of a complex mixture of early- and later-formed pyrite reworked from the overlying strata—along with pyrite formed at the same time as formation of the LPM (Formolo and Lyons, 2007). The latter would reflect dominantly low but dynamic oxygen conditions in the bottom waters, including the likelihood of intermittent euxinia (Sageman and Lyons, 2003; Formolo and Lyons, 2007).

Samples were collected from the outcrop at Fall Brook of the Leicester pyrite member (42°53’60’’N, 78°29’32’’W) (outcrop location provided in the Supplementary Information (SI), Fig. S1). To avoid surface oxidation, samples were taken tens of centimeters into the outcrop and those in the interior of the hand specimen were selected for analyses. Samples were mounted in epoxy and polished to a final of 1 µm diameter.

2.2 Analytical protocols

A nodule containing several individual framboids was located using a combination of reflected light microscopy and SEM (Fig. S2a). The texture of the pyrite framboids was resolved by chemical-imaging by nanoscale secondary ion mass spectrometry (NanoSIMS), using a CAMECA NanoSIMS 50L. Prior to analysis, samples were coated with 10 nm of high purity Ir to improve conductivity. All images reported

here were collected as two frames consisting of 256 × 256 pixels collected with a dwell time of 13.5 ms pixel^{-1}. NMR magnetic field regulation was employed in all cases. Negative secondary ion images were collected using a 16 keV Cs^+ primary ion beam. Secondary ions were accelerated to 8 keV and were collected using electron multipliers. Prior to image analysis, image areas were pre-sputtered with about 2 × 10^{16} ions cm^{-2} Cs^+. Ion images of $^{12}C_2^-$ and $^{34}S^-$ were collected using a 2pA, primary beam that had a diameter of approximately 120 nm. Analysis of the images was performed using OpenMIMS and ImageJ (Abramoff et al., 2004). Consecutive frames were deadtime corrected on a pixel × pixel basis, aligned, and summed.

Select framboids of interest were analyzed by APT and/or STEM , based on their paragenesis as described below. Specimens were prepared using a dual-beam SEM (Thermo Fisher Scientific Helios Nanolab 600i) using conventional focused ion beam (FIB) capabilities (Giannuzzi and Stevie, 1999; Thompson et al., 2007) (see SI for further details, Fig. S1) and mounted onto Si half- grids (Dune Sciences, OR, USA).

TEM was performed with aberration-corrected FEI Titan 80-300 operated at 300 kV to characterize the pyrite and inclusion microstructure. The microscope incorporates CEOS GmbH double-hexapole aberration corrector for the probe-forming lens, which allows imaging with ~0.8 nm resolution in STEM mode. The presented images were acquired in STEM mode using a high-angle annular dark-field detector with beam convergence of 17.8 mrad and collection angle of 54 mrad. All images were acquired with TIA software package.

APT specimens were analyzed in a CAMECA Local Electrode Atom Probe (LEAP 4000 X-HR) at a set-point temperature of 40 K, a laser pulse repetition rate of 125 kHz, and a detection rate of 0.004-0.005 ions per pulse (maintained by varying the applied specimen voltage). The laser wavelength was 355 nm, and laser energy per pulse was 40 pJ. The data were reconstructed using the Integrated Visualization and Analysis Software (IVAS 3.8.5) developed by CAMECA. An average atomic volume of 0.013nm^3 atom^{-1} was specified in the 3D reconstruction, representing the atomic density in the pyrite lattice (i.e., ~75 atoms nm^{-3}). Reconstructions were based on images and measurements of the tip profile, adjusting the image compression factor to better match tip radii. A voxel size of 1.0 × 1.0 × 1.0 nm and delocalization of 3.0 × 3.0 × 3.0nm was applied.

A detailed description of the APT analytical procedure is provided in the SI, to which the reader is referred to for more detail. In brief, the specimen chemistry was reconstructed by assigning ionic species to each mass-to-charge state peak in the generated spectra to best reproduce the expected elemental and isotopic compositions. Elemental compositions and ratios were calculated relative to the ion counts

detected within the measured volume. Analyses were conducted on a museum-grade pyrite specimen as a standard sample (see SI), providing reliable elemental measurements on the LPM. A total of four APT specimens from a single framboid in the LPM were analyzed by both STEM and APT, all of which observed similar general structural and chemical features at the nanoscale. One specimen is described in detail in the main text as a representative sample.

To identify fluid inclusions, ion segregation/clustering was probed via various APT techniques. Elemental distributions were visualized to gain firsthand observations for clustering. To quantitatively confirm and describe the extent to which ions segregate and cluster, statistical analyses and random comparator techniques were conducted (see SI for additional details) (Stephenson et al., 2007; Perea et al., 2015; Taylor et al., 2018). In brief, using nearest neighbor (NN) analyses, the distances between designated solute ions in the experimental specimen were measured and compared to that for a simulated dataset where ions are randomly distributed. The tendency for an ion to cluster was determined by quantifying the deviation in the NN distributions between the experimental and simulated datasets based on the Pearson coefficient μ (calculation in SI), where if μ=0 the solute distribution is completely random while if μ=1 the distribution is non-random and the ions are spatially associated, consistent with that expected for inclusions. Point density variations were also observed using 2D heat maps to confirm the identified clusters were consistent with previous APT descriptions for fluid inclusions (Dubosq et al., 2020).

3. Results and Discussion

3.1 Identification of nanoscale fluid inclusions

3.2 Pyrite framboid paragenesis

For this study, it was of particular interest to probe pyrite framboids that formed in the water column, as we postulate these are more likely to archive seawater compositions at their time of formation—in contrast to diagenetic pyrite which forms in the sediments within pore waters that may be shifted dramatically in composition from the overlying waters. Some of the pyrite from the LPM was previously deduced to be water-column derived from analyses using Mo as a proxy for formation conditions (Gregory, 2020). In brief, using LA-ICPMS, Mo concentrations measured within small pyrite framboids (<10 um) ranged from 80 to 400. Both the small sizes and Mo enrichments are consistent with environments reflecting euxinic deposition (Gregory et al., 2022). The Mo contents of the LPM samples were also at least an order of magnitude higher than those of framboids deposited under modern oxic water columns (median values range from 5-40 ppm) (Gregory et al., 2014); see Formolo and Lyons (2007) for additional evidence of euxinic deposition). Thus, it is expected that some material from the LPM can preserve seawater conditions from the initial formation time.

A nodule containing several individual framboids was imaged by NanoSIMS to resolve the framboid texture more clearly and further infer its formation conditions (Figure 1a). The framboids were generally shown to be <10 µm in diameter and to consist of clusters of pyrite microscopic crystals. The presence of these smaller framboids suggests their likely formation in the sulfidic (euxinic) water column (Wilkin et al., 1996). The framboidal texture is also indicative of pyrite formation at a high degree of supersaturation (Rickard, 2012) that usually forms very early, either in the water column or early during sedimentation (Rickard 2019, 2021; Wilkin et al., 1996). Pyrite formed later in sedimentation due to diffusional overprint is usually coarser grained (Gregory et al., 2022). Metamorphic recrystallization is also coarser grained and non-framboidal (Large et al., 2011; Large et al., 2009).

3.1.1 Microstructural and chemical characterization

Framboids on the outer edge of the nodule with the specified characteristics were targeted for microstructural characterization using high-resolution STEM (Figure 1a). High-resolution imaging highlights the assemblage of numerous sub-micrometer scale crystals (~400 nm in diameter) with well-formed (euhedral) crystal faces forming framboids, bound together with a nano-porous pyrite cement (Figure 1b). Furthermore, nanoscale low-density features are found to be littered within the primary pyrite grain; the features are typically <4 nm in size and are mostly spherical in shape (a fraction also appears ellipsoidal). The features are densely packed with a spacing typically <2 nm, although the actual distance can deviate given the nature of the image as a 2D projection; this was also evaluated by 3D APT (discussed shortly).

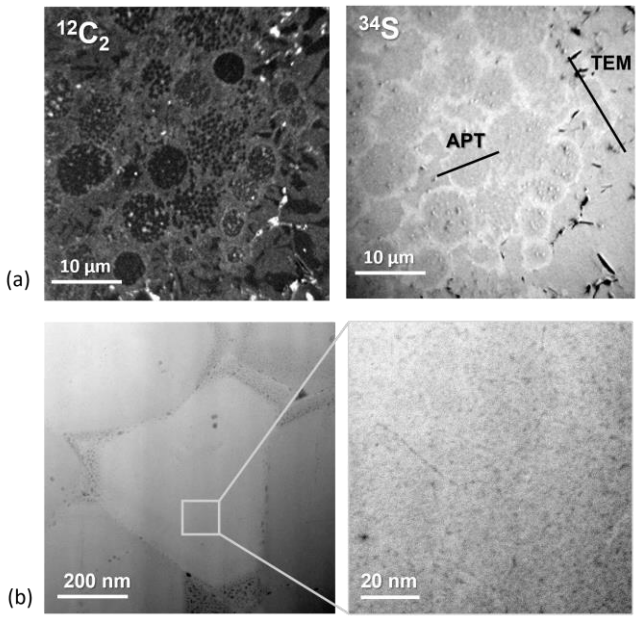

Figure 1: Diagnostic features for the Leicester pyrite member. (a) Chemical mapping with NanoSIMS of $^{12}C_2$ and ^{34}S species, denoting the framboids specifically probed by STEM and APT. (b) STEM imaging of framboids (marked as TEM in panel "a")

consisting of euhedral pyrite nanoparticles within a porous, disordered pyrite matrix. Low-density regions exist at the nanoscale in the crystalline pyrite bulk.

APT specimens were prepared from a nearby framboid with similar characteristics (Figure 1b, Fig. S2), and analyzed by both STEM and APT to directly correlate structural and chemical features at the nanoscale, respectively. STEM imaging of a tip shows the nanoscale, low-density features scattered within crystalline pyrite (Figure 2a), consistent with the nanotexture observed in primary grains, i.e., the features were mostly spherical in morphology with an average diameter of ~3 nm and appear densely packed. APT compositional analyses indicates that the chemistry is consistent with that expected for pyrite (e.g., the samples averaged ~35 atomic % (at.%) Fe and ~61 at.% S compared to 33at.% and 67at.% for stoichiometric pyrite, respectively). Visualization of the distribution of Fe and S ions shows they are homogeneously distributed in the specimen, indicating the major element chemistry of the pyrite matrix is consistent across the specimen (Figure 2b).

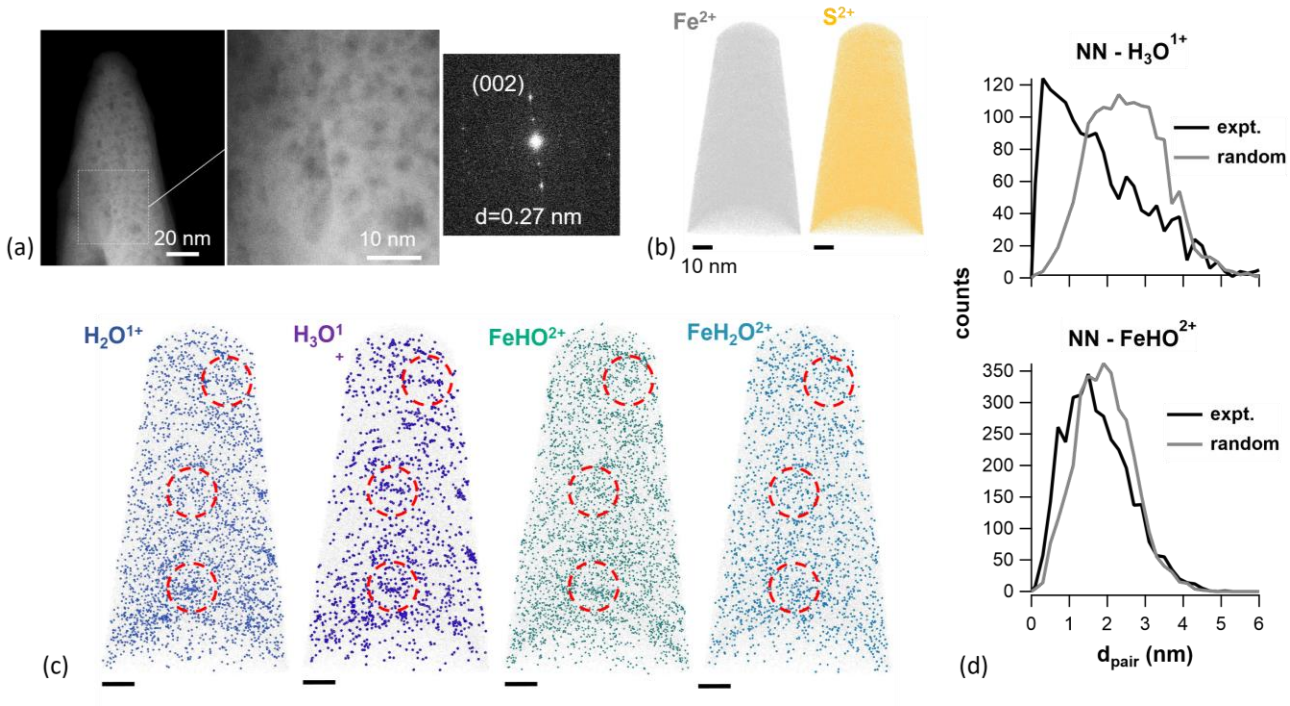

Figure 2: Correlative STEM/APT analysis showing inclusions within pyrite from the LPM specimen. (a) STEM imaging of APT specimen showing the presence of low-density regions in pyrite. Correlative fast fourier transform analysis shows lattice diffraction spots corresponding to (002) planes in pyrite (lattice spacing of 0.27 nm), confirming the specimen crystallinity. APT atomic maps showing the distribution of (b) Fe^{2+} and S^{2+} ionic-species and (c) hydrated species H_2O^{1+}, H_3O^{1+}, $FeHO^{2+}$, and FeH_2O^{2+}. Red circles are used to correlate the distributions to specific regions. Ion sizes are exaggerated for clarity. (d) NN analyses for H_3O^{1+} compared to $FeHO^{2+}$.

Interestingly, several impurities including hydrated species, alkalis (i.e., Na, Mg, K, and Ca), and nonmetal species (i.e., organics as well as Se and Br) are present (Figure 3a, b). Identification was aided through analysis of a pyrite standard (see SI for more details, Fig. S2) and referring to previous APT characterizations of this mineral , and confirm these impurities are unique to the LPM specimens. The detection of hydrated ionic species in the form of hydroxide and iron-hydroxide ions is particularly interesting, as they suggest the presence of water in the specimen. That is, H_2O^{1+} and H_3O^{1+} species at 18-19 Da (collectively referred to as H_xO species) are readily measured and account for ~0.7% of all ionic species measured within the pyrite tips (averaged across the four APT specimens analyzed), while $FeHO^{2+}$ and FeH_2O^{2+} species at 35.5-38Da (FeH_xO species) account for ~0.6% of all ionic species. While APT is a solid-phase characterization technique and cannot directly probe pure liquid states, the presence of related hydrated ionic-species can be used to infer the presence of aqueous components (Schreiber et al., 2018; El-Zoka et al., 2020; Liu et al., 2022). These signatures are similar to those observed in a hydrated fayalite, where APT analyses showed H_xO and FeH_xO species localized within nanoscale defects (Liu et al., 2022).

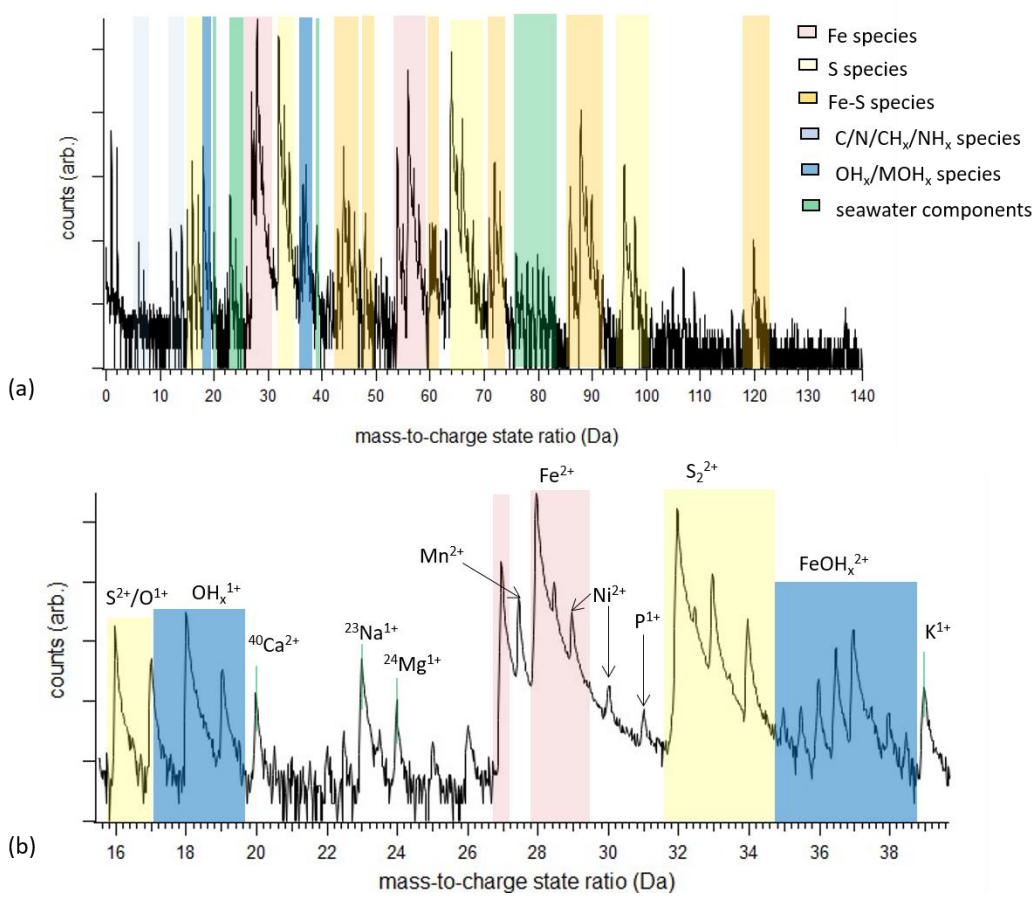

Figure 3: (a) APT mass spectra for LPM highlighting the various ionic species present. Though not of direct interest to this study, the seawater components at the 76 – 82 Da are Se and Br. (b) Mass peaks highlighting hydrated and major alkali ionic species of interest to this study. Counts are shown on a logarithmic scale.

3.1.2 Cluster analysis

Identification and characterization of nanoscale fluid inclusions within the pyrite matrix by APT was enabled through various cluster analysis techniques. Given the clear presence of hydrated ionic species, the distribution of H_xO and FeH_xO ions were visualized in 3D to observe ion segregation/clustering that would be consistent with the nature of ions in fluid inclusions. In particular, H_xO-ions were readily observed as clusters within the pyrite matrix (Figure 2c). FeH_xO-ions also appear to cluster to some extent although this was more ambiguous based on visual inspection alone.

To better inform observations for ion clustering/segregation and in turn identify species representative of inclusions, statistical analyses were conducted. For instance, NN analyses show H_3O^{1+} ions are within spatial proximity to one another compared to the simulated dataset where ion distributions are randomized (i.e., the modes for the inter-ionic distances measured are 0.3 nm vs. 2.3 nm, respectively) (Figure 2d).

The deviation in the NN distributions between the experimental and simulated datasets is significant (μ = 0.9) and confirms strong clustering, consistent with that expected for ions associated with inclusions. In comparison, NN analyses of shows $FeHO^{1+}$ also clusters but less strongly than H_3O^{1+} (i.e., modes for the inter-ionic distances were 1.4 nm vs. 1.9 nm, respectively, with μ = 0.39). Overall, statistical analyses across the four specimens consistently showed H_xO-species to strongly cluster (average μ for H_2O^{1+} and H_3O^{1+} are 0.7 and 0.9, respectively) compared to FeH_xO-ions (average μ for $FeHO^{2+}$ and FeH_2O^{2+} are 0.5 and 0.3, respectively) (Figure 2c, d; Table S1). In turn, these analyses complement direct observations of the elemental distributions and enable us to reliably deduce nanoscale fluid inclusions based on H_xO species.

Morphological/structural characterization of the inclusions by APT is qualitatively similar to that observed for the low-density features by STEM. That is, 3D visualization of H_xO clusters as isosurfaces shows the inclusions are typically ~1 – 10 nm in diameter and the morphology is spherical to oblate (Figure 4a). These observations are nominally consistent to that from STEM, although structural information at the sub-nanometer scale is limited due to inherent spatial aberrations and distortions resulting from the analysis of chemically complex nanostructures by APT (Vurpillot et al., 2000; Marquis and Vurpillot, 2008; Devaraj et al., 2014; Perea et al., 2016; Dubosq et al., 2020). Each cluster consists of ~10 to ~200 H_xO-ions, with the number of clusters varying among the APT tips from ~ 60 – 100 (select clusters are shown in Figure 4a for clarity). The clusters are typically densely-packed with spacings of ~ 2 – 5 nm, although less densely-packed regions are also present. The clusters are also shown to be consistent with fluid inclusions based on 2D ion density maps (Figure 4b); i.e., the higher ion density in the inclusion compared to the matrix is due to the concave shape of the inclusion walls focusing ion evaporation paths and low-field constituents in the inclusions evaporating faster, as observed in previous APT studies (Dubosq et al., 2020). Thus, combined with the observations of nanoscale low-density features within the pyrite from correlative STEM imaging, this study presents strong evidence for nanoscale water-filled inclusions within pyrite.

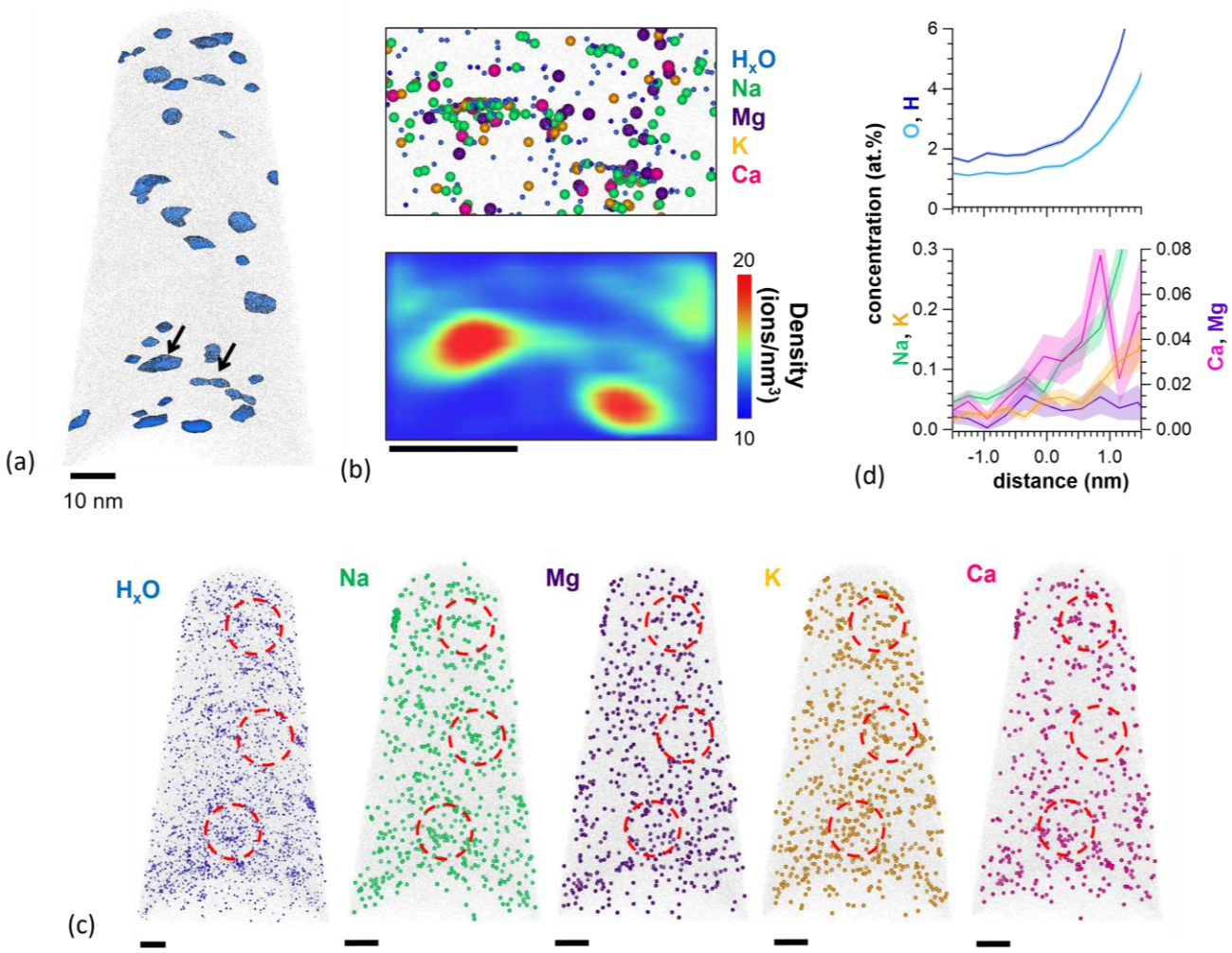

Figure 4: (a) Isosurfaces showing morphology of select inclusions (2 ion% H_xO). (b) Correlative atomic and point density maps for inclusions denoted by black arrows in panel (a). (c) Atomic maps visualizing the distribution of H_xO, Na, Mg, K, and Ca species across the specimen. Ion sizes are exaggerated for clarity. Gray atoms are Fe representing the pyrite matrix. Red circles are used to correlate the distribution to specific regions. (d) Volumetric compositional analysis within H_xO-isosurfaces showing the elemental distribution of alkalis in inclusions (positive distances) relative to the matrix (negative distances). Error is represented by the shaded error bands (1σ, see SI for calculation); note, the error for O and H is more subtle due to the larger measurement scale.

3.3 Evaluation of seawater chemistry

In addition to water, several alkali and alkaline elements (i.e., Na, Mg, K, and Ca) were also observed (Figure 3b). These ions were visualized across the APT tips and were found to largely exist in clusters, with subtle variations in their spatial distributions (Figure 4b, c). For example, Na, K, and Ca strongly cluster, while Mg also clusters but not as strongly (further supported by statistical analyses in Table S1; average μ = 0.9, 0.7, 0.7, and 0.5, respectively). The ions also appear largely associated with the fluid inclusions. That is, compositional measurements within the H_xO-cluster volumes show that the alkalis are

more concentrated within the inclusions compared to the matrix (Figure 4d), e.g., Na decreases an order of magnitude from >0.3 at.% in the inclusion to ~0.05 at.% in the matrix while Mg shows a more subtle decrease from ~0.02 at.% to ~0.01 at.%.

The alkalis detected are consistent with major cations found in seawater and thus suggest that remnants of (paleo)seawater may have been entrained within the pyrite during growth. In an effort to assess whether the elemental signature of the water column in which the framboids formed is captured and preserved, we quantified the alkali ion concentrations associated with the fluid inclusions in our sample and compared this to previously predicted compositions for seawater in the Devonian, based on measurements from halite inclusions (Horita et al., 2002) as well as models (Demicco et al., 2005). Concentrations are expressed as ratios relative to Ca.

Table 1: Alkali compositional measurements from the inclusions across the four APT specimens. Specimen 3 is the representative specimen shown in Figures 2 – 4. Measurements are compared to those from previous studies including [§]Horita et al. (2002) and [‡]Demicco et al. (2005). For Demicco et al. (2005), a range of values for the elemental ratios are provided based on estimations from all four models tested. The error within individual specimens is represented by the uncertainty (2σ; 95% confidence interval) while the error in the average across the tips is represented by the standard deviation (2SD).

		Predicted water-column chemistry		
		Mg/Ca	**K/Ca**	**Na/Ca**
		0.8-0.9, <1.5[§] ~0.5 – 1.4[‡]	~0.3 – 0.8[‡]	~10 – 21[‡]
		Measured inclusion chemistry *(± 2σ)*		
LPM specimen	**# atoms collected**	**Mg/Ca**	**K/Ca**	**Na/Ca**
1	1.76×10^{6}	0.52 ± 0.13	1.52 ± 0.29	3.53 ± 0.60
2	2.25×10^{6}	0.87 ± 0.20	1.87 ± 0.34	4.15 ± 0.70
3	3.96×10^{6}	0.52 ± 0.10	1.60 ± 0.24	3.25 ± 0.43
4	1.38×10^{6}	0.50 ± 0.17	1.77 ± 0.43	5.67 ± 1.18
Average composition (± 2SD)		***0.60 ± 0.15***	***1.69 ± 0.14***	***4.15 ± 0.94***

Mg/Ca measurements from the inclusions in the LPM specimen (averaging 0.6±0.2 across the four APT specimens) are in reasonable agreement with that predicted for the Middle Devonian (i.e., ~0.8-0.9, with a maximum of 1.5, based on direct measurement of inclusions by Horita et al. (2002) or within ~0.5 – 1.4, based on models by Demicco et al. (2005)) (Table 1). Measurements across the four specimens were generally consistent and within error of one another.

Although measurements of K and Na concentrations are not well-established for the Devonian and are poorly constrained across geologic time in general, we probed their concentrations within the inclusions as a secondary check. In contrast to Mg, measurements for K and Na from the LPM deviate from those predicted in previous studies by modelling. That is, K is overestimated with respect to modelled values during the Devonian (Demicco et al., 2005) (average K/Ca for LPM 1.7±0.1 *vs.* ~0.3 – 0.8 , respectively) while Na is instead underestimated (i.e. 4.2±0.9 vs. ~10 – 21, respectively).

While the ratios of Na and K deviate quantitatively from predicted values, we speculate the qualitative trends for Na and K may correlate to the expected brine composition and marine evaporite for the period. That is, Mg/Ca measurements here are consistent with that predicted for the Middle Devonian where paleoseawater is depleted in Mg and elevated in Ca, especially relative to present-day seawater compositions (i.e., Mg/Ca = 5.2) (Hardie, 1996; Lowenstein et al., 2001). At low Mg/Ca (i.e., < 2.0), calcite is the dominant non-skeletal carbonate while KCl is the dominant evaporite (whereas aragonite and $MgSO_4$ are dominant when Mg/Ca > 2.0, as in present-day conditions), loosely correlating to the higher K concentrations measured here. Similarly, the lower Na concentrations here may correlate to analyses of paleoseawaters with low Mg/Ca (e.g., from the Cambrian, Silurian, and Cretaceous) where Na was relatively depleted during halite precipitation compared to that at high Mg/Ca, like present-day halite-saturated seawater brines.

The alkali composition in the bulk (i.e., the entire specimen including the matrix and inclusions) was compared to assess whether potential mass transfer reactions could have influenced compositional analyses of the inclusions. In general, alkali compositions are nominally consistent between the inclusions and the bulk, i.e., average Mg-, K-, and Na/Ca in the bulk are 0.9±0.3, 1.6±0.2, and 3.4±0.6 (see SI, Table S2), within error of that measured in the inclusions (Table 1). It is possible processes like incorporation and/or diffusion occur, e.g., higher Mg/Ca in the bulk indicates a fraction of Mg is associated within the pyrite matrix in addition to the inclusions (consistent with our statistical analyses as well, Table S1). However, it is uncertain whether this would arise from diffusion between inclusions and the matrix or if ions are incorporated in the pyrite lattice during crystallization, as knowledge of these phenomena for alkali ions in pyrite is lacking; controlled and systematic experiments combined with modelling (beyond the scope of this paper) would provide valuable insight into these behaviors (Cherniak, 2010; Evans et al., 2020; Mavromatis et al., 2022). Overall, the comparable compositions between the inclusions and bulk indicate mass transfer between the inclusion with the matrix is not significant. Further, measurements for Mg/Ca within the inclusions are in reasonable agreement with that predicted to the Devonian (Horita et al., 2002; Demicco et al., 2005) and suggest paleo seawater signatures are effectively preserved.

4. Conclusions

This study presents new insight into the microstructural and chemical characterization of nanoscale fluid inclusions as well as their potential to explore paleoenvironmental conditions, enabled through correlative analyses using high-resolution techniques. Specifically, analyses were conducted on pyrite framboids from the middle-Devonian LPM formation with textures indicative of early-stage formation in a sulfidic (euxinic) water column, based on NanoSIMS characterization. Correlative STEM and APT analyses revealed the presence of nanoscale water-filled inclusions, as low-density features (typically <4 nm) homogenously scattered within the pyrite matrix and distinct clusters of hydrated ionic-species were directly observed. Further, unique chemical signatures consistent with water-column chemistry were readily detected and included major ions from seawater (i.e., Na, Mg, K, and Ca). Quantification of the alkali concentrations indicate that the fluid inclusions contain marine salinities consistent with those hypothesized for the Middle Devonian, particularly Mg/Ca measurements (Demicco et al., 2005). These combined observations provide strong evidence that these pyrite regions are petrographically primary and have not undergone significant recrystallization or infiltration of diagenetic or metamorphic fluids.

The potential to resolve paleoseawater signatures and compositions through analyses of nanoscale features offers exciting opportunities. For example, this approach can be applied to access more thorough records of Mg/Ca may aid in tracking the occurrence of calcite versus aragonite seas across geologic time. Oscillations between a dominance of aragonite versus calcite in abiotic marine $CaCO_3$ precipitates throughout Earth history are closely coupled to the evolution of seawater composition more broadly and provide the environmental context for biomineralization of calcareous organisms (Folk and Land, 1975; Hardie, 1996; Lowenstein et al., 2001). $CaCO_3$ polymorph formation is linked to distinct Mg/Ca and temperature-dependent thresholds, with calcite forming at low temperatures and relatively low Mg/Ca (< 2.0), while aragonite forms at warm temperatures under higher Mg/Ca (> 2.0). Our measured Mg/Ca within the LPM specimen averaged 0.6±0.2, consistent with predictions of calcite seas dominating the Middle Devonian and independent estimates of Mg/Ca (~0.8-0.9) (Lowenstein et al., 2001; Horita et al., 2002). The great abundance of pyritic euxinic shales through time elevates the temporal utility of the approach.

Continued technical development in the analyses of nanoscale fluid inclusions is needed, including evaluation of the chemical/structural nature of these features across a broader range of specimens of pyrite and within different minerals. It would be of particular interest to probe the chemistry of early-formed, pervasive-growth pyrite nodules relative to later-formed pyrite nodules reflecting concentric-growth mechanisms; these may provide a window into the chemistry of ancient ocean bottom waters where the latter may track the evolution of pore waters that have become partly or completely isolated

from seawater (Gregory et al., 2019). The approach developed here is also more broadly applicable; for example, analyses of pyrite ores could provide salinity estimates for ore-related fluids and thus constrain genetic models. In turn, the ability to probe and characterize nanoscale fluid inclusions can potentially provide unprecedented insight into ancient paleoenvironments and the chemical evolution of diverse subsurface fluids, even in samples with complicated histories of mineralization and alteration.

5. Acknowledgements

Sample preparation and LEAP 4000 XHR analyses were performed using Environmental and Molecular Sciences Laboratory, a national scientific user facility sponsored by the DOE Office of Biological and Environmental Research and located at PNNL. We thank Jeffery Over and Stephanie Olson for help during sample of the Leicester pyrite member. We further acknowledge funding through EMSL proposal 49860 to Lyons and NSERC Discovery Grant funding to Gregory.

6. Supplementary Information

Additional information on methodology and analytical procedures are provided in the separate Supplementary Information attachment.

7. Data availability

The authors declare that all the necessary data supporting the findings of this study are available in the article and its Supplementary Information files. Due to ongoing research utilizing this data, raw data files can be made available from the corresponding authors upon request.

8. Author Contributions

SDT and DEP were involved in specimen preparation, APT analysis, and data interpretation. LK was involved in TEM analysis. JBC was involved in SIMS analysis. DDG and TWL were involved sample acquisition, characterization, study design, and data interpretation. SDT, DDG, and TWL were involved in manuscript preparation.

9. Competing Interests Statement

The authors declare that there are no competing interests.

10. References

Goldstein, R.H., 2001. Clues from fluid inclusions. Science 294, 1009-1011.

391 Lowenstein, T.K., Timofeeff, M.N., Brennan, S.T., Hardie, L.A., Demicco, R.V., 2001. Oscillations in
392 Phanerozoic seawater chemistry: Evidence from fluid inclusions. Science 294, 1086-1088.
393 Balthasar, U., Cusack, M., 2015. Aragonite-calcite seas—Quantifying the gray area. Geology 43, 99-102.
394 Brennan, S.T., Lowenstein, T.K., 2002. The major-ion composition of Silurian seawater. Geochim. et
395 Cosmochim. Acta 66, 2683-2700.
396 Johnson, W.J., Goldstein, R.H., 1993. Cambrian seawater preserved as inclusions in marine low-
397 magnesium calcite cement. Nature 362, 335-337.
398 Bodnar, R.J., Samson, I., 2003. Introduction to fluid inclusions, Fluid inclusions: Analysis and
399 interpretation, pp. 1-8.
400 Viti, C., Frezzotti, M.-L., 2001. Transmission electron microscopy applied to fluid inclusion investigations.
401 Lithos 55, 125-138.
402 Deditius, A.P., Utsunomiya, S., Ewing, R.C., Kesler, S.E., 2009. Nanoscale "liquid" inclusions of As-Fe-S in
403 arsenian pyrite. Amer. Mineral. 94, 391-394.
404 Parish, C.M., Field, K.G., Certain, A.G., Wharry, J.P., 2015. Application of STEM characterization for
405 investigating radiation effects in BCC Fe-based alloys. Journal of Materials Research 30, 1275-1289.
406 Marquis, E.A., Vurpillot, F., 2008. Chromatic aberrations in the field evaporation behavior of small
407 precipitates. Microsc. and Microanaly. 14, 561-570.
408 Marquis, E.A., Hyde, J.M., 2010. Applications of atom-probe tomography to the characterisation of
409 solute behaviours. Mat Sci Eng R 69, 37-62.
410 Gault, B., Chiaramonti, A., Cojocaru-Mirédin, O., Stender, P., Dubosq, R., Freysoldt, C., Makineni, S.K., Li,
411 T., Moody, M., Cairney, J.M., 2021. Atom probe tomography. Nature Reviews Methods Primers 1, 51.
412 Fougerouse, D., Reddy, S.M., Saxey, D.W., Rickard, W.D.A., van Riessen, A., Micklethwaite, S., 2016.
413 Nanoscale gold clusters in arsenopyrite controlled by growth rate not concentration: Evidence from
414 atom probe microscopy. Amer. Mineral. 101, 1916-1919.
415 Taylor, S.D., Liu, J., Arey, B.W., Schreiber, D.K., Perea, D.E., Rosso, K.M., 2018. Resolving iron(II) sorption
416 and oxidative growth on hematite (001) using atom probe tomography. J. Phys. Chem. C 122, 3903-
417 3914.
418 Taylor, S.D., Liu, J., Zhang, X., Arey, B.W., Kovarik, L., Schreiber, D.K., Perea, D.E., Rosso, K.M., 2019.
419 Visualizing the iron atom exchange front in the Fe(II)-catalyzed recrystallization of goethite by atom
420 probe tomography. P. Natl. Acad. Sci. USA 116, 2866-2874.
421 Moser, D.E., Chamberlain, K.R., Tait, K.T., Schmitt, A.K., Darling, J.R., Barker, I.R., Hyde, B.C., 2013.
422 Solving the Martian meteorite age conundrum using micro-baddeleyite and launch-generated zircon.
423 Nature 499, 454-457.
424 Valley, J.W., Cavosie, A.J., Ushikubo, T., Reinhard, D.A., Lawrence, D.F., Larson, D.J., Clifton, P.H., Kelly,
425 T.F., Wilde, S.A., Moser, D.E., Spicuzza, M.J., 2014. Hadean age for a post-magma-ocean zircon
426 confirmed by atom-probe tomography. Nat. Geosci. 7, 219-223.
427 Peterman, E.M., Reddy, S.M., Saxey, D.W., Snoeyenbos, D.R., Rickard, W.D.A., Fougerouse, D., Kylander-
428 Clark, A.R.C., 2016. Nanogeochronology of discordant zircon measured by atom probe microscopy of Pb-
429 enriched dislocation loops. Sci. Adv. 2, 1601318.
430 White, L.F., Darling, J.R., Moser, D.E., Reinhard, D.A., Prosa, T.J., Bullen, D., Olson, D., Larson, D.J.,
431 Lawrence, D., Martin, I., 2017. Atomic-scale age resolution of planetary events. Nat. Comm. 8, 15597.
432 Dubosq, R., Gault, B., Hatzoglou, C., Schweinar, K., Vurpillot, F., Rogowitz, A., Rantitsch, G., Schneider,
433 D.A., 2020. Analysis of nanoscale fluid inclusions in geomaterials by atom probe tomography:
434 Experiments and numerical simulations. Ultramicroscopy 218, 113092.
435 Reddy, S.M., Saxey, D.W., Rickard, W.D.A., Fougerouse, D., Montalvo, S.D., Verberne, R., van Riessen, A.,
436 2020. Atom probe tomography: Development and application to the geosciences. Geostand. Geoanaly.
437 Res. 44, 5-50.

Daly, L., Lee, M.R., Hallis, L.J., Ishii, H.A., Bradley, J.P., Bland, P.A., Saxey, D.W., Fougerouse, D., Rickard, W.D.A., Forman, L.V., Timms, N.E., Jourdan, F., Reddy, S.M., Salge, T., Quadir, Z., Christou, E., Cox, M.A., Aguiar, J.A., Hattar, K., Monterrosa, A., Keller, L.P., Christoffersen, R., Dukes, C.A., Loeffler, M.J., Thompson, M.S., 2021. Solar wind contributions to Earth's oceans. Nature Astronomy 5, 1275-1285.
Dubosq, R., Rogowitz, A., Schneider, D.A., Schweinar, K., Gault, B., 2021. Fluid inclusion induced hardening: nanoscale evidence from naturally deformed pyrite. Contributions to Mineralogy and Petrology 176, 15.
Liu, J., Taylor, S.D., Qafoku, O., Arey, B.W., Colby, R., Eaton, A., Bartrand, J., Shutthanandan, V., Manandhar, S., Perea, D.E., 2022. Visualizing the distribution of water in nominally anhydrous minerals at the atomic scale: Insights from atom probe tomography on fayalite. Geophys Res Lett 49.
Formolo, M.J., Lyons, T.W., 2007. Accumulation and preservation of reworked marine pyrite beneath an oxygen-rich devonian atmosphere: Constraints from sulfur isotopes and framboid textures. J. Sediment. Res. 77, 623-633.
Horita, J., Zimmermann, H., Holland, H.D., 2002. Chemical evolution of seawater during the Phanerozoic: Implications from the record of marine evaporites. Geochim. et Cosmochim. Acta 66, 3733-3756.
Demicco, R.V., Lowenstein, T.K., Hardie, L.A., Spencer, R.J., 2005. Model of seawater composition for the Phanerozoic. Geology 33, 877-880.
Baird, G.C., Brett, C.E., 1986. Erosion on an anaerobic seafloor: Significance of reworked pyrite deposits from the Devonian of New York State. Paleogeogr., Paleocl., Paleoec. 57, 157-193.
Sageman, B.B., Lyons, T.W., 2003. Geochemistry of fine-grained sediments and sedimentary rocks, in: Holland, H.D., Turekian, K.K. (Eds.), Treatise on Geochemistry. Pergamon, Oxford, pp. 115-158.
Abramoff, M.D., Magalhaes, P.J., Ram, S.J., 2004. Image processing with ImageJ. Biophon. Intl. 11, 36-42.
Giannuzzi, L.A., Stevie, F.A., 1999. A review of focused ion beam milling techniques for TEM specimen preparation. Micron 30, 197-204.
Thompson, K., Lawrence, D., Larson, D.J., Olson, J.D., Kelly, T.F., Gorman, B., 2007. *In situ* site-specific specimen preparation for atom probe tomography. Ultramicroscopy 107, 131-139.
Stephenson, L.T., Moody, M.P., Liddicoat, P.V., Ringer, S.P., 2007. New techniques for the analysis of fine-scaled clustering phenomena within atom probe tomography (APT) data. Microsc. and Microanaly. 13, 448-463.
Perea, D.E., Arslan, I., Liu, J., Ristanovic, Z., Kovarik, L., Arey, B.W., Lercher, J.A., Bare, S.R., Weckhuysen, B.M., 2015. Determining the location and nearest neighbours of aluminium in zeolites with atom probe tomography. Nat. Comm. 6.
Gregory, D.D., 2020. The pyrite trace element paleo-ocean chemistry proxy. Cambridge University Press, Cambridge.
Gregory, D.D., Lyons, T.W., Large, R.R., Stepanov, A.S., 2022. Ground-truthing the pyrite trace element proxy in modern euxinic settings. Amer. Mineral. 107, 848-859.
Gregory, D., Meffre, S., Large, R., 2014. Comparison of metal enrichment in pyrite framboids from a metal-enriched and metal-poor estuary. Amer. Mineral. 99, 633-644.
Wilkin, R.T., Barnes, H.L., Brantley, S.L., 1996. The size distribution of framboidal pyrite in modern sediments: An indicator of redox conditions. Geochim. et Cosmochim. Acta 60, 3897-3912.
Schreiber, D.K., Perea, D.E., Ryan, J.V., Evans, J.E., Vienna, J.D., 2018. A method for site-specific and cryogenic specimen fabrication of liquid/solid interfaces for atom probe tomography. Ultramicroscopy 194, 89-99.
El-Zoka, A.A., Kim, S.H., Deville, S., Newman, R.C., Stephenson, L.T., Gault, B., 2020. Enabling near-atomic-scale analysis of frozen water. Sci. Adv. 6.
Vurpillot, F., Bostel, A., Blavette, D., 2000. Trajectory overlaps and local magnification in three-dimensional atom probe. Appl. Phys. Lett. 76, 3127-3129.

Devaraj, A., Colby, R., Vurpillot, F., Thevuthasan, S., 2014. Understanding atom probe tomography of cxide-supported metal nanoparticles by correlation with atomic-resolution electron microscopy and field evaporation simulation. J. Phys. Chem. Lett. 5, 1361-1367.
Perea, D.E., Liu, J., Bartrand, J., Dicken, Q., Thevuthasan, S.T., Browning, N.D., Evans, J.E., 2016. Atom probe tomographic mapping directly reveals the atomic distribution of phosphorus in resin embedded ferritin. Sci. Rep. 6, 22321.
Hardie, L.A., 1996. Secular variation in seawater chemistry: An explanation for the coupled secular variation in the mineralogies of marine limestones and potash evaporites over the past 600My. Geology 24, 279-283.
Cherniak, D.J., 2010. Diffusion in carbonates, fluorite, sulfide minerals, and diamond. Rev Mineral Geochem 72, 871-897.
Evans, D., Gray, W.R., Rae, J.W.B., Greenop, R., Webb, P.B., Penkman, K., Kröger, R., Allison, N., 2020. Trace and major element incorporation into amorphous calcium carbonate (ACC) precipitated from seawater. Geochim. et Cosmochim. Acta 290, 293-311.
Mavromatis, V., Brazier, J.-M., Goetschl, K.E., 2022. Controls of temperature and mineral growth rate on Mg incorporation in aragonite. Geochim. et Cosmochim. Acta 317, 53-64.
Folk, R.L., Land, L.S., 1975. Mg/Ca ratio and salinity: Two controls over crystallization of dolomite. AAPG Bull. 59, 60-68.
Gregory, D., Mukherjee, I., Olson, S.L., Large, R.R., Danyushevsky, L.V., Stepanov, A.S., Avila, J.N., Cliff, J., Ireland, T.R., Raiswell, R., Olin, P.H., Maslennikov, V.V., Lyons, T.W., 2019. The formation mechanisms of sedimentary pyrite nodules determined by trace element and sulfur isotope microanalysis. Geochim. et Cosmochim. Acta 259, 53-68.